Molecular engineering of dispersed nickel phthalocyanines on carbon nanotubes for selective CO_2 reduction

Xiao Zhang[1,2], Yang Wang[1], Meng Gu[1], Maoyu Wang[3], Zisheng Zhang[4], Weiying Pan[1], Zhan Jiang[1], Hongzhi Zheng[1], Marcos Lucero[3], Hailiang Wang[5,6], George E. Sterbinsky[7], Qing Ma[8], Yang-Gang Wang[4,*], Zhenxing Feng[3,*], Jun Li[4,9], Hongjie Dai[2], Yongye Liang[1,10,*].

[1]Department of Materials Science and Engineering, Southern University of Science and Technology, Shenzhen 518055, China.

[2]Department of Chemistry, Stanford University, Stanford, California 94305, USA.

[3]School of Chemical, Biological, and Environmental Engineering, Oregon State University, Corvallis, OR, 97331, USA.

[4]Department of Chemistry, Guangdong Provincial Key Laboratory of Catalysis, Southern University of Science and Technology, Shenzhen 518055, China.

[5]Department of Chemistry, Yale University, New Haven, Connecticut 06520, USA.

[6]Energy Sciences Institute, Yale University, West Haven, Connecticut 06516, USA.

[7]Advanced Photon Source, Argonne National Laboratory, Argonne, IL 60439, USA.

[8]DND-CAT, Synchrotron Research Center, Northwestern University, Evanston, IL 60208, USA.

[9]Department of Chemistry, Tsinghua University, Beijing 100084, China.

[10]Guangdong-Hong Kong-Macao Joint Laboratory for Photonic-Thermal-Electrical Energy Materials and Devices, Southern University of Science and Technology, Shenzhen 518055, China.

*Correspondence should be addressed to: liangyy@sustech.edu.cn; zhenxing.feng@oregonstate.edu; wangyg@sustech.edu.cn.

X.Z., Y.W., M.G., and M.W. contributed equally to this work.

Abstract

Electrochemical reduction of CO_2 is a promising route for sustainable production of fuels. A grand challenge is developing low-cost and efficient electrocatalysts that can enable rapid conversion with high product selectivity. Here we design a series of nickel phthalocyanine molecules supported on carbon nanotubes as molecularly dispersed electrocatalysts (MDEs), achieving CO_2 reduction performances superior to aggregated molecular catalysts in terms of stability, activity, and selectivity. The optimized MDE with methoxy group functionalization solves the stability issue of the original nickel phthalocyanine catalyst and catalyzes the conversion of CO_2 to CO with > 99.5% selectivity at high current densities up to -300 mA cm^{-2} in a gas-diffusion electrode device with stable operation at -150 mA cm^{-2} for 40 h. The well-defined active sites of MDEs also facilitate the in-depth mechanistic understandings from *in-situ/operando* X-ray absorption spectroscopy and theoretical calculations on structural factors affecting electrocatalytic performance.

Harvesting electricity from renewable energy sources and then using electrons to drive chemical transformations is an appealing scheme for sustainable production and regeneration of carbon-based chemicals and fuels[1,2]. Electrocatalysts are indispensable for this transformation to afford lower energy losses and higher efficiencies[3,4], and demand high activity and stability based on earth-abundant elements[5-7]. However, developing such electrocatalysts still remains a major challenge[8,9]. For example, commonly used electrocatalysts for carbon dioxide reduction reaction (CO_2RR) to carbon monoxide (CO), which could be readily incorporated to produce value-added chemicals[10,11], still rely on noble metals such as gold (Au)[12] or silver (Ag)[13], especially for operations at high current densities. At current densities > 150 mA cm^{-2}, selectivities decreased below 90%[14,15]. Higher product selectivity is preferred to simplify product purification and enhance energy conversion efficiency[16].

Recently, atomically dispersed transition metals embedded in nitrogen doped carbon matrices (M-N-C) have emerged as competitive candidates for CO_2RR[17,18]. These M-N-C catalysts are generally synthesized by high-temperature pyrolysis and it is difficult to precisely control the structures of active sites and further improve performance. Molecular complexes with nitrogen coordinated metal centers (*e.g.*, metal phthalocyanine, MePc, and metal porphyrin) have attracted significant interest as catalysts for CO_2RR because of their structural uniformity and tunability[19-22]. Very recently, cobalt phthalocyanine (CoPc) molecules were reported to catalyze CO_2RR to CO at 50 mA cm^{-2} for several hours with selectivities > 95% in a zero-gap membrane flow reactor[23]. For most molecular catalysts in heterogeneous form, catalytic performances are often limited by their nonconducting and aggregating nature, leading to

low reduction current densities[24,25]. Cobalt phthalocyanines and porphyrins were supported on conductive nanocarbon materials to afford higher current densities[22,26-28], but this strategy has been less explored for designing molecules containing other metals with well-defined active sites for CO_2RR applications and/or mechanistic investigations[29,30]. Iron and nickel phthalocyanines were hybridized with carbon nanotubes for CO_2RR but showed inferior selectivities to their cobalt counterparts under large overpotentials[30].

In this work, we develop a series of molecularly dispersed electrocatalysts (MDEs) based on designed nickel phthalocyanine (NiPc) molecules, affording CO_2RR to CO with > 99% selectivities and long-term stability at high current densities. These MDEs are constructed by supporting highly dispersed, non-aggregated NiPc molecules on multi-walled carbon nanotubes (MWCNTs, simplified as CNTs in the following text). By engineering the pendant groups on Pc, a stable NiPc-OMe-MDE with methoxy (OMe) group functionalization is identified. NiPc-OMe-MDE exhibits stable performance at -150 mA cm^{-2} and 0.50 V overpotential with > 99.5% selectivity to CO for 40 h in a gas-diffusion electrode (GDE) device, which is more active, selective, and stable than previous molecular electrocatalysts. The well-defined structures of these MDEs are also beneficial for mechanistic insight studies, facilitating the understanding of how molecular structures affect catalytic activity and stability.

Molecular design and CO_2RR performance of NiPc-MDEs

Ni-N-C catalysts prepared by pyrolysis were reported to drive selective CO_2RR to generate CO[17,31-34], and different coordination environments of the Ni active sites (Ni-N_x)

were proposed[17,33,34]. NiPc is a large conjugated molecule containing a Ni-N_4 moiety in the first coordination shell and has been reported as a moderate electrocatalyst for reducing CO_2 to CO[35]. We synthesized an electron-donating methoxy group substituted NiPc, nickel(II) 2,9(10),16(17),23(24)-tetrakis(methoxy)phthalocyanine (NiPc-OMe), and an electron-withdrawing cyano group substituted NiPc, nickel(II) 2,3,9,10,16,17,23,24-octacyano-phthalocyanine (NiPc-CN) (Fig. 1a for molecular structures, Methods and Supplementary Fig. 1 for details of synthesis and characterizations) to explore the role of pendant group functionalization of NiPc. We found that micrometer sized aggregates were usually formed when directly depositing NiPc on substrates by drop drying (Supplementary Fig. 2)[19], and the low conductivity and aggregating nature often afforded poor catalytic performance[36]. To overcome this problem, we anchored the original and substituted NiPc molecules on the sidewalls of CNTs through π-π stacking to achieve molecular dispersion of NiPcs on conducting CNT sidewalls (Fig. 1a), preventing molecular aggregation and facilitating efficient charge transfer to the active sites. The NiPc-MDEs were made by ultrasonically mixing the respective dimethylformamide (DMF) suspensions of NiPc molecules and CNTs (see Methods for details), and the Ni loadings were all determined to be 0.76±0.03 wt.% (determined by inductively coupled plasma mass spectrometry, ICP-MS).

Well dispersed molecules on the sidewalls of CNTs (outer diameters of ~12 nm) were observed in NiPc-MDEs free of observable aggregation of NiPcs (Supplementary Fig. 3) using high resolution aberration-corrected scanning transmission electron microscopy (STEM). Z-contrast high angle annular dark field (HAADF) images showed isolated bright spots (size ~0.24 nm) on CNT sidewalls (Fig. 1b and Supplementary Fig. 4),

confirmed to be Ni^{2+} by the Ni *L* edge signal in electron energy loss spectroscopy (EELS, Fig. 1B inset). Energy-dispersive X-ray spectroscopy (EDS) elemental mappings further supported that Ni and N in the NiPc molecules were uniformly distributed on CNTs (Supplementary Fig. 5). These results confirmed molecular dispersion of original and substituted NiPcs containing $Ni-N_4$ sites on CNTs, which could be served as model Ni-N-C catalysts with well-defined structures.

The NiPc-MDEs were deposited on carbon fiber paper (CFP) substrates with a 0.4 mg cm^{-2} catalyst loading to be measured in a gas-tight H-cell for CO_2RR. All potentials were converted to versus reversible hydrogen electrode (RHE) with *iR* corrections. In a CO_2-saturated 0.5 M $KHCO_3$ electrolyte, cathodic currents were observed from linear sweep voltammetry (LSV) with an onset potential (where the reduction current density reaches 0.1 mA cm^{-2}) of -0.43 V using NiPc-MDE (Fig. 1c and Supplementary Fig. 6). In contrast, neat NiPc (directly deposited on CFP from a DMF suspension without supporting on CNTs) with the same metal loading (0.03 mg cm^{-2} of NiPc) showed no appreciable electrocatalytic activity, similar to blank CFP substrates (Supplementary Fig. 7). Increasing the neat NiPc loading to 0.4 mg cm^{-2} improved activities, but still much lower than NiPc-MDE (Supplementary Fig. 7). The low activity of the neat NiPc electrodes can be attributed to the aggregation of NiPc molecules (Supplementary Fig. 2) and consequently fewer exposed active sites and inferior electron transport from the electrode to the active site to drive the reaction. Introducing electron-withdrawing cyano groups to prepare NiPc-CN-MDE afforded a positive shift of 50 mV in the onset potential (Supplementary Fig. 6) and improved CO_2RR activities compared to NiPc-MDE (Fig. 1c). Although electron-donating methoxy-substituted NiPc-OMe-MDE showed a slightly

more negative onset potential (Supplementary Fig. 6), its activities became higher than NiPc-MDE at more negative potentials (Fig. 1c).

Chronoamperometric measurements were carried out at different potentials to obtain product distributions. CO was the only gaseous product from CO_2RR with H_2 as the by-product from hydrogen evolution reaction (HER). Faradaic efficiencies of CO and H_2 [FE(CO)s and FE(H_2)s] from NiPc-MDEs were plotted in Fig. 1d and Supplementary Fig. 8, respectively. In the reduction current density range of ~1.5 to ~22 mA cm^{-2} (where mass transport limitation of CO_2 is not significant)[37], FE(CO)s of the NiPc-MDEs were greater than 96%, suggesting high CO selectivity of CO_2RR. With the NiPc-OMe-MDE, impressive FE(CO)s higher than 99% throughout the current density range (potential range of -0.54 to -0.68 V) were obtained (Fig. 1d). To compare, we synthesized a pyrolyzed Ni-N-C catalyst with atomically dispersed Ni (P-NiNC)[33] and observed lower reduction currents and lower FE(CO)s (*e.g.,* ~90% at -0.62 V) compared to the NiPc-MDE under identical testing conditions (Fig. 1c,d and Supplementary Fig. 9). This was likely due to the competing HER active sites generated during high-temperature treatment of pyrolyzed catalyst[18].

The stability of CO_2RR by NiPc-MDEs were also investigated by chronoamperometric measurements. The original NiPc-MDE exhibited unstable electrocatalytic performance especially at high reduction current densities (Fig. 1e and Supplementary Fig. 10a). Note that the previously reported inferior FE(CO)s of NiPc hybridized with CNTs to the CoPc counterpart at more negative potentials (< -0.8 V vs. RHE)[30] could be attributed to this fast deactivation of original NiPc at high reduction current densities. Similar decay was also observed in pyrolyzed Ni-N-C catalysts[17,31,32]. The NiPc-CN-MDE, though operated

at lower overpotentials, still suffered from stability issue (Fig. 1e and Supplementary Fig. 10b). In contrast, the methoxy group substituted NiPc-OMe-MDE exhibited much higher stability in the CO_2RR activities at reduction current densities up to 22.3 mA cm^{-2} (Fig. 1e and Supplementary Fig. 10c). These results showed that pendant group functionalization of NiPc molecules can tune the electrocatalytic activity, selectivity, and stability of NiPc-MDEs. Through molecular synthesis/screening and dispersing/anchoring on CNTs, we identified methoxy functionalized NiPc-OME-MDE for active, selective, and stable CO_2RR (Supplementary Table 1).

NiPc-MDEs in gas-diffusion electrodes

To investigate high-current performance for the CO_2RR electrolyzer, we incorporated NiPc-MDEs to fabricate gas-diffusion electrodes (GDEs) (Supplementary Fig. 11 for experimental setup and Methods for details). GDE benefits from the fast diffusion of CO_2 through gas-phase to the catalyst, instead of through electrolyte in conventional H-cells, to improve the mass transfer during reaction and afford large operation current (> 150 mA cm^{-2}) for CO_2RR[6,38,39]. The GDE cell included a vigorously stirred liquid electrolyte at the cathode compartment to ensure well-mixed electrolyte and enable three-electrode measurements to reveal the CO_2RR performance of the catalysts. NiPc-MDEs were coated on the microporous gas-diffusion layers (GDLs) with a 1.0 mg cm^{-2} catalyst loading and 1.0 M $KHCO_3$ was used as electrolyte. The GDE with NiPc-OMe-MDE can be operated at current densities from -10 to -400 mA cm^{-2} with modest overpotentials (Fig. 2a and Supplementary Fig. 12a). Remarkably high FE(CO)s of > 99.8% were obtained from -10 to -300 mA cm^{-2} (Fig. 2b, Supplementary Fig. 13 and Supplementary

Table 2 for performance summary at various current densities). Note that polytetrafluoroethylene (PTFE) was incorporated into the catalyst layer to render hydrophobicity and enhance the diffusion of CO_2 to the active sites to achieve high reduction current densities (Supplementary Fig. 14). Addition of PTFE to electrodes of neat MePcs slightly increased the CO_2RR selectivity and overpotentials compared to electrodes prepared without PTFE, but stable operations at reduction current densities > 100 mA cm^{-2} still could not be achieved in both cases (Supplementary Fig. 15), inferior to their MDE counterparts.

Generally, the selective electrocatalysts for CO_2RR to CO reported previously showed FE(CO)s < 97% at moderate current densities (Supplementary Table 3 for comparison with previous reports), and significantly lower selectivities at low current densities and high current densities (Fig. 2b)[14,15,40-42]. For example, the FE(CO)s of a pyrolyzed Ni-N-C catalyst dropped to below 80% beyond 250 mA cm^{-2} [41], and an Au-based catalyst exhibited FE(CO)s below 83% and 90% at current densities < 25 and > 300 mA cm^{-2}, respectively[40]. The high selectivities over a wide range of current densities obtained with NiPc-OMe-MDE [FE(CO)s > 99% from -10 to -400 mA cm^{-2}] were enabled by the high intrinsic selectivities together with the well-defined structures of the Ni-N_4 sites, which is exceptional and unprecedented compared to reported CO_2RR to CO catalysts. Long-term operation at -150 mA cm^{-2} with NiPc-OMe-MDE showed stable potentials at around -0.61 V for 40 h and FE(CO)s of > 99.5% were maintained during the whole process (Fig. 2c). This performance was better than the reported FE(CO)s of ~90% with a carbonate-derived Ag catalyst in 1 M KOH electrolyte (requiring refreshing electrolyte around every 20 h) for 100 h[14] and decreasing FE(CO)s from ~88% to 80% in 20 h with a

pyrolyzed Ni-N-C catalyst[41] at similar current densities. At -400 mA cm^{-2}, flooding of NiPc-OMe-MDE electrodes by the electrolyte was observed, resulting in large fluctuation of the voltage and slight decrease of FE(CO)s to 99.1% in the 40 min measurement (Supplementary Fig. 12a and Supplementary Table 2). Prolonged operation at -400 mA cm^{-2} resulted in electrode failure due to the flooding issue, which could be solved by improved design of GDE structures to enable stable operation at even higher current densities[6]. Although NiPc-CN-MDE exhibited lower overpotentials than NiPc-OMe-MDE at reduction current densities < 200 mA cm^{-2} (Fig. 2a), its activities and selectivities decayed in less than 3 h at -150 mA cm^{-2} (Supplementary Fig. 16).

The turnover frequency (TOF) of NiPc-OMe-MDE at -150 mA cm^{-2} was calculated to be 12 s^{-1} assuming all the Ni sites were electrocatalytically active, a record TOF value at similar current densities and much higher than the reported TOF of ~0.22 s^{-1} with aggregated CoPc[23]. Although exhibiting slightly higher performance than neat NiPc-based molecules (Supplementary Figs. 17,18,19, possibly due to better charge transport), neat CoPc tested in identical conditions was inferior to NiPc-OMe-MDE (Fig. 2a,b). Molecular modification of CoPc showed slight enhancement in performance, which could be operated at -75 mA cm^{-2} for 10 h with increasing overpotentials[43]. Dispersing CoPc on CNTs to synthesize CoPc-MDE also enhanced the activities compared to aggregated molecules (Supplementary Fig. 20), but the product selectivity and stability was still inferior to NiPc-OMe-MDE, showing that FE(CO)s decreased from ~97% to below 90% in 20 h at -150 mA cm^{-2} (Supplementary Fig. 21). With the high activities, selectivities, and stabilities of NiPc-OMe-MDE at large current densities, it could be readily incorporated into practical CO_2RR electrolyzers (Supplementary Table 3).

225

226 **Mechanistic insights of NiPc-MDEs**

227 Supporting NiPc molecules on CNTs allows for molecular dispersion of well-defined
228 active sites for electrocatalysis and facilitates evolutions of the catalysts since the highly
229 dispersed molecules are electrochemically accessible. Otherwise aggregated
230 heterogeneous molecular catalysts are difficult for elucidating the correlation of
231 molecular structure and catalytic activities (as in neat NiPc, NiPc-OMe, NiPc-CN,
232 Supplementary Fig. 18). To understand how molecular engineering modulates the
233 electrocatalytic properties of NiPc-MDEs, we conducted *in-situ/operando* X-ray
234 absorption spectroscopy (XAS) measurements[44,45] and density-functional theory (DFT)
235 calculations to investigate the electronic structures and catalytic behaviors of NiPc-
236 MDEs.

237 Cyclic voltammetry (CV) of NiPc-MDEs were first performed in Ar-saturated 0.1 M
238 phosphate buffer (PB, pH=7.4) electrolyte to characterize the electrochemical behavior of
239 original and substituted NiPc-MDEs without the impact from CO_2RR intermediates. Two
240 reduction peaks at -0.01 and -0.64 V, respectively, were observed on NiPc-MDE
241 (Supplementary Fig. 22). The second reduction peak of NiPc-CN-MDE shifted positively
242 to -0.22 V, while negatively shifted to -0.69 V on NiPc-OMe-MDE. Both the first and
243 second reduction peaks of NiPc molecules were assigned to ligand reduction according to
244 previous reports[46]. The occurrence of the second reduction peaks in our NiPc-MDEs
245 coincided with the onset of CO_2RR activities, suggesting reduced NiPc molecules
246 responsible for the CO_2RR activities.

The molecular dispersion of catalyst molecules in the MDEs provides an excellent platform to investigate the real active sites by *in-situ/operando* XAS since most of the metal centers with well-defined structures were electrochemically accessible. *In-situ* X-ray absorption near edge structure (XANES) spectra at Ni *K*-edge of NiPc-MDE showed a small shift of ~0.75 eV to lower energy in the rising edge region (~8344 eV) when holding at -0.68 V in Ar-saturated 0.1 M PB compared to those at open-circuit voltage (OCV) and -0.37 V (Fig. 3a), indicating that the first reduction located on the phthalocyanine ligand and the second reduction was partially on Ni centers. Band edge shifts to lower energy were also observed at -0.37 and -0.72 V with NiPc-CN-MDE and NiPc-OMe-MDE (Fig. 3a and Supplementary Fig. 23). The partially reduced Ni centers from *in-situ* XANES spectra (Supplementary Fig. 23) and the positive/negative shifts of reduction peaks from CV scans (Supplementary Fig. 22) suggested the successful tuning of the Ni electron density with the introduction of electron-withdrawing/donating groups.

NiPc-MDEs were further characterized in CO_2-saturated 0.5 M $KHCO_3$ electrolyte to gain information under the CO_2RR condition. The XANES and its first derivative spectra of NiPc-MDE showed slight band edge shift to lower energy (~8346 eV) upon operation of CO_2RR at -0.53 V (~ -1 mA cm^{-2}) and became more obvious at -0.68 V (~ -5 mA cm^{-2}) compared to that at OCV (Fig. 3b,c), suggesting a partial reduction of the Ni center. The pre-edge peak at ~8336 eV, a signature of the square-planar Ni-N_4 structure in NiPc[47], were weakened under both -0.53 V and -0.68 V, indicating structural distortion of the Ni-N_4 sites[48]. An additional component at ~1.9 Å (no phase correction) in the Fourier transforms of the extended X-ray absorption fine structure spectra (EXAFS-FT) was observed at -0.68 V (Supplementary Fig. 24d), which was not observed from the same

catalyst in the CO_2-free PB electrolyte at -0.68 V (Supplementary Fig. 25). Quantitative fitting of the EXAFS spectra in R space suggested four Ni-N bonds (bond length of 1.91 Å) together with one new Ni-C bond at 2.06 Å under CO_2RR condition at -0.68 V (Supplementary Table 4 and Supplementary Fig. 26). The new Ni-C bond can be assigned to adsorbed reaction intermediates on the Ni centers[32]. The ratio of the coordination numbers of the Ni-N and Ni-C bonds was ~4, indicating that most of the Ni centers had an adsorbed intermediate under steady state of CO_2RR.

More profound change was found on NiPc-CN-MDE operated at -0.58 V (~ -5 mA cm^{-2}). The pre-edge peak at ~8336 eV disappeared and the first EXAFS-FT peak split into a doublet under this condition (Fig. 3b and Supplementary Fig. 24e), suggesting significant distortion from/decomposition of the Ni-N_4 structure during CO_2RR. Holding the electrode at OCV after reaction only partially restored the spectral shape and the pre-edge peak compared to the fresh NiPc-CN-MDE electrode (Supplementary Fig. 24b), indicating an irreversible degradation of the Ni centers. Such decomposition could be the origin of instability of the NiPc-MDE and NiPc-CN-MDE catalysts (Supplementary Fig. 27)[49]. In contrast, only slight changes in the oxidation state and coordination environment of the Ni centers were observed when holding NiPc-OMe-MDE at -0.53 and -0.65 V with current densities of ~ -1 and -5 mA cm^{-2}, respectively (Fig. 3b,c and Supplementary Fig. 24c,f), indicating its resistance to structural changes. This is consistent with its better electrochemical stability.

Kohn-Sham molecular orbital analysis revealed that the doubly degenerated lowest unoccupied molecular orbitals (LUMOs) of NiPc were mainly located on the Pc ligand with minor contribution from the Ni center (Fig. 4a and Supplementary Fig. 28). Our

theoretical results were consistent with the small change of Ni oxidation state observed in *in-situ*/*operando* XAS with the formation of reduced NiPc molecules. The LUMO energy level of NiPc shifted down from -2.70 eV to -4.63 eV with the introduction of electron-withdrawing cyano groups and shifted up to -2.40 eV with electron-donating methoxy groups (Fig. 4a), agreeing with the observed order of reduction potentials from CV scans. In addition, Mulliken population analysis indicated the creation of electron-rich and electron-deficient environments of Ni in NiPc-OMe and NiPc-CN compared to NiPc, respectively (Supplementary Fig. 29).

The Gibbs free energy diagram of CO_2RR on NiPc from DFT calculations showed that the adsorption of CO_2 on the active Ni center was accompanied by a proton-coupled electron transfer (PCET) step to generate *COOH, which was the rate-determining step (RDS). *COOH experienced a following PCET step to form *CO and then desorbed to regenerate the free active site (Fig. 4b). The reduction of NiPc, coupled with proton transfers to generate NiPc-H and NiPc-H_2, markedly facilitated the RDS due to the stabilization of *COOH, revealing the correlation between the formation of reduced NiPc catalysts and CO_2RR activities (Supplementary Fig. 30). Although NiPc-OMe-H_2 showed the lowest energy required to generate *COOH from the free energy diagram, NiPc-CN-H_2 was generated with the least negative potential and exhibited the highest initial activities in CO_2RR[50]. To be specific, the needed overpotential to drive the reaction relied on the reduction of NiPc molecules rather than the free energy change of elementary steps with NiPc catalysts, indicating the limitations of interpreting the activities of molecular catalysts solely based on calculated free energy diagram. Furthermore, the calculated highly positive free energy change required for the formation of adsorbed

hydrogen intermediate during HER (Supplementary Fig. 31) suggested the preferred high selectivities towards CO_2RR of NiPc-MDEs. In addition, the calculated Ni-C bond length of CO adsorbed on reduced NiPc (2.04 Å, Supplementary Fig. 26c) was consistent with the new Ni-C bond (2.06 Å) observed from quantitative fitting of the EXAFS spectra of NiPc-MDE under CO_2RR (Supplementary Table 4).

Analysis of Ni-N bond orders in NiPc molecules showed that NiPc-OMe possessed the strongest Ni-N bonds (Fig. 4c), consistent with the resistance to structural changes during CO_2RR of NiPc-OMe-MDE observed in *operando* XAS (Fig. 3b). The strengthened Ni-N bonds and favored CO desorption (Fig. 4b) with methoxy substituents can synergistically enhance the electrochemical stability of NiPc-OMe-MDE and make it a stable CO_2RR catalyst.

With the help of *in-situ/operando* XAS and DFT calculations, knowledge of how ligand groups affect the properties of the active Ni centers was obtained. The electron-withdrawing CN groups decrease the electron density on the Ni centers, which facilitates the formation of a reduced active center to enhance the electrocatalytic activities of NiPc-CN-MDE at low overpotentials. But it still suffers from decaying activities due to structural instability at high overpotentials. In contrast, the electron-donating OMe groups enhance the Ni-N bond strength in the $Ni-N_4$ sites and accelerate CO desorption compare to the original NiPc-MDE to improve the catalyst stability, a critical figure of merit for practical CO_2RR electrolyzer. The OMe substitution also stabilizes the *COOH intermediate to further enhance the selectivity towards CO_2RR over HER.

Conclusions

Molecular dispersion of NiPc molecules unlocked the remarkable electrocatalytic properties for CO_2RR from molecular aggregates. With the fine-tuning of pendant groups on the Pc ligand, NiPc-OMe-MDE exhibited FE(CO)s > 99.5% over a wide current density range of -10 to -300 mA cm^{-2} and stable performance at practically relevant -150 mA cm^{-2} for 40 h. These results also emphasize that MDE cooperating with molecular engineering such as pendant group functionalization is a powerful strategy in designing affordable catalysts for critical electrochemical transformations.

Methods

Synthesis of NiPc-OMe

The synthesis followed a two-step procedure with modifications[51,52]. 4-Nitrophthalonitrile (4 g) and 10 ml of methanol were added to 60 ml of N,N-dimethylformamide (DMF), followed by adding potassium carbonate (K_2CO_3, 8 g). The reaction mixture was then heated to 70 °C and kept for 3 h with magnetic stirring and Ar protection. The black mixture was then partitioned between water (150 ml) and dichloromethane (DCM, 150 ml). The aqueous phase was separated and extracted with DCM (200 ml × 3). The solvents of combined organic phase were removed under reduced pressure and the product was purified by flash chromatography with DCM as eluent to give 4-methoxyphthalonitrile (2.7 g, 73% yield). In the next step, 4-methoxyphthalonitrile (2.7 g) and nickel acetate tetrahydrate (1.35 g) were added to a Schlenk flask equipped with a stir bar, followed by adding 50 ml of sulfolane. After several cycles of vacuum and refilling with Ar, 1,8-diazabicyclo[5.4.0]undec-7-ene (DBU, 0.6 ml) was added, followed by another three cycles of vacuum and refilling with

Ar. The reaction mixture was heated to 160 °C and kept for 10 h. The reaction mixture was precipitated from methanol (400 ml) and the collected solid was subjected to Soxhlet extraction. The solid was further extracted by DMF for several times and the solvent of combined DMF solutions was removed to obtain NiPc-OMe (600 mg, 18% yield). ESI-mass (*m/z*): 690.12458 (M^+). Analysis: $C_{36}H_{24}O_4N_8Ni$, 690.12685.

Synthesis of NiPc-CN

The synthesis followed a one-step procedure with modifications[53]. 1,2,4,5-Tetracyanobenzene (1.0 g) and nickel acetate tetrahydrate (0.4 g) were added to a Schlenk flask equipped with a stirring bar, followed by adding 20 ml of sulfolane. After several cycles of vacuum and refilling with Ar, DBU (0.2 ml) was added, followed by another three cycles of vacuum and refilling with Ar. The reaction mixture was heated to 135 °C and kept for 6 h. The reaction mixture was precipitated from methanol (400 ml) and the collected solid was subjected to Soxhlet extraction. The solid was further extracted by DMF for several times and the solvent of combined DMF solutions was removed to yield NiPc-CN (410 mg, 38% yield). ESI-mass (*m/z*): 770.04838 (M^+). Analysis: $C_{40}H_8N_{16}Ni$, 770.04768.

Preparation of MePc MDEs

NiPc and CoPc were obtained from Alfa Aesar. To prepare MePc MDEs, 30 mg CNTs (C-Nano, FT 9000) were dispersed in 20 ml DMF by high-power sonication for 1 h (Xinzhi SB-5200D, 360 W). A calculated amount of the original or substituted NiPc/CoPc was dissolved in 10 ml DMF with high-power sonication and added to the CNT suspension. The mixed suspension was sonicated for another 30 min and stirred at

room temperature for 24 h. NiPc has low solubility in DMF, so the high-power sonication step is important for mixing. The MePc-MDE materials were separated by centrifuge and washed with DMF, ethanol, and water (Milli-Q water with a resistivity of 18.2 MΩ cm at 25 °C was used throughout the experiments), followed by lyophilization to obtain the final products.

Synthesis of P-NiNC

The synthesis adopted a previous report with minor modifications[33]. Briefly, zinc nitrate hexahydrate (0.9 g) and nickel nitrate hexahydrate (0.9 g) were dissolved in 120 ml methanol. The solution was than mixed with 2-Methylimidazole (2-MeIm, 2.0 g dissolved in 40 ml methanol) and stirred at room temperature for 18 h. The reaction mixture was centrifuged at 8000 rpm for 6 min to collect the precipitate, which was further washed with methanol for three times and dried in a vacuum oven at 80 °C overnight. The solid was subjected to heat treatment at 1000 °C (ramping rate of 5 °C min^{-1}) in a tube furnace for 3 h under 100 standard cubic centimeters per minute (sccm) Ar flow. The black power was used directly without any further treatments.

Material characterizations

Scanning transimission electron microscopy (STEM) was performed on a double Cs-aberration-corrected FEI Themis G2 microscope at 60kV with super-X EDS and Quantum EELS spectrometer. Transmission electron microscopy (TEM) was conducted with a FEI Tecnai G2 F30 transmission electron microscope. Scaning electron microscopy (SEM) was conducted on a TESCAN MIRA3 LM model. Inductively coupled plasma mass spectrometry (ICP-MS) was performed on an Agilent Technologies 7700 series instrument. High-resolution mass spectrometry (HR-MS) was performed on

Q-Exactive. Ultraviolet-visible (UV-Vis) spectromotry was performed with a Shimadzu UV3600 spectrometer.

Electrochemical measurements

All electrochemical measurements were carried out with a CHI 760E potentiostat and a Bio-Logic VSP potentiostat (for impedance measurements). A three-electrode configuration was used for CO_2RR measurements. All potentials were recorded against an Ag/AgCl (filled with saturated KCl solution) reference electrode and converted to versus RHE with *iR* corrections by the following equation:

$$E_{vs.RHE} = E_{vs.Ag/AgCl} + 0.0591 \cdot pH + 0.197 - i \cdot R_u$$

where i is the average current and R_u is the solution resistance.

Gas outlet of the cathodic compartment was connected to an on-line gas chromatograph (GC, SRI Instruments MG#3) with a gas-sampling loop (1 ml) for product quantification. The GC was equipped with a packed molecular sieve 13X column and a HAYESEP-D column with N_2 (99.999%) as the carrier gas. A flame ionization detector (FID) with a methanizer was used to quantify CO fraction and a thermal conductivity detector (TCD) was used to quantify H_2 fraction. Faradaic efficiencies (FEs) of CO from the CO_2RR was calculated with gas fractions of CO referencing to peak areas of standard gas mixtures (0.5% CO). FEs of H_2 was calculated with gas fractions of H_2 referencing to H_2 production with a Pt mesh electrode in 0.1 M $HClO_4$ electrolyte (Supplementary Fig. 13). FEs of CO and H_2 were obtained by the following equations:

$$FE = \frac{2 \cdot g \cdot x \cdot p \cdot F}{i \cdot R \cdot T}$$

where g is the CO_2 flow rate , x is the fraction of CO or H_2 detected by GC, p is 101325 Pa, F is 96487 C mol^{-1}, i is the current measured by the potentiostat, R is 8.314 J mol^{-1} K^{-1}, and T is 273.15 K.

All current densities were calculated using the geometric area of electrodes. TOFs were calculated based on the catalyst loading on substrates and metal contents of catalysts, assuming that all metal sites were electrochemically accessible. This should be the lower limit of the real TOF values. The reported FEs and TOFs are average values based on at least three measurements. The reported linear sweep voltammograms and chronoamperograms are representative data for these runs. The currents in chronoamperograms were recorded ~3 minutes after applying potentials to reach steady state.

The H-cell setup consisting of a gas-tight two-compartment electrochemical cell separated by an anion-exchange membrane (Selemion DSV) was described in detail previously[22]. To prepare the electrodes of MDEs, 100 µl catalyst ink (prepared by dispersing 2.0 mg catalyst in a mixture of 170 µl 0.5 wt.% Nafion solution and 830 µl ethanol with the assistance of sonication) was drop-coated on CFP (Toray, TGP-H-060) to cover an active area of 0.5 × 1.0 cm^2 (loading: 0.4 mg cm^{-2}). Neat NiPc electrodes were prepared by directly depositing from the DMF suspension on CFP to achieve the same metal loading as in the NiPc-MDE electrode (0.03 mg cm^{-2}) or a catalyst loading of 0.4 mg cm^{-2}. A graphite rod and an Ag/AgCl electrode were used as the counter and reference electrodes, respectively. 0.5 M $KHCO_3$ solutions pre-saturated with CO_2 were used as electrolytes (35 ml of electrolyte in cathodic/anodic chambers with ~20 ml headspace). A high-purity CO_2 (99.999%) gas flow at 5 sccm was delivered into the

cathodic compartment and kept during reaction. The electrodes were pre-scanned from 0 V to -1.5 V vs. the Ag/AgCl refernece electrode (without *iR* compensation) at 200 mV/s for ~80 cycles or electrolyzed at -1.5 mA cm^{-2} for 40 min to activate catalysts. For EIS experiments, the catalyst ink was deposited on a glassy carbon electrode (5.0 mm in diameter) to achieve a loading of ~0.2 mg cm^{-2}. Spectra were recorded at potentials where -0.5 mA cm^{-2} current densities were achieved with that catalyst in the H-cell with an amplitude of 5.0 mV and frequency range of 100 kHz to 0.01 Hz.

A three-compartment (gas, cathodic, and anodic chambers) home-made electrochemical cell (Supplementary Fig. 11) was used to conduct three-electrode gas-diffusion electrode (GDE) experiments. The diameter of roundness window for electrolysis was set to 0.8 cm, yielding the active area of 0.50 cm^2. To prepare the electrodes of MDEs, 8.0 mg of the catalyst material was dispersed in 3.6 ml ethanol with 16 µl 5.0 wt.% Nafion solution and 400 µl 1.0 wt.% PTFE solution (diluted from a 60 wt.% stock solution with water) with sonication for 1 h. A certain amount of the catalyst ink was drop-coated on a 1.5 × 1.5 cm^2 gas-diffusion layer (GDL, SGL25BC) with a 1.0 mg cm^{-2} catalyst loading. The electrodes were then heated at 330 °C for 1 h under Ar to remove the surfactant in the PTFE solution. To prepare electrodes with neat metal phthalocyanines, 2.0 mg of the molecules was dispersed in a mixture of 170 µl 0.5 wt.% Nafion solution and 830 µl ethanol with the assistance of sonication and a certain amount of the catalyst ink was drop-coated on the 1.5 × 1.5 cm^2 GDL to achieve a 1.0 mg cm^{-2} catalyst loading. A piece of copper tape or titanium foil was used as current collectors for the CO_2RR cathodes. The side of cathodes with deposited catalysts faced the electrolyte. A graphite rod and an Ag/AgCl electrode (inserted in the cathodic chamber) were used as

474 the counter and reference electrodes, respectively. The cathodic and anodic chambers
475 were separated by an anion-exchange membrane (Selemion DSV). 1.0 M $KHCO_3$ pre-
476 saturated with argon was used as the electrolyte. The electrolyte in the cathodic chamber
477 (~20 ml) was vigorously stirred to minimize the thickness of diffusion layer. Correction
478 of *iR* drop (resistance of ~7 Ω) was applied to the measured potentials to extract the real
479 working potentials of the CO_2RR cathodes and eliminate the impact of GDE cell design
480 to allow for comparison with other catalysts. To accurately quantify the FEs of CO and
481 H_2 under large reduction currents, Ar was used as the carrier gas for GC to detect both
482 CO and H_2 with TCD to avoid the non-linear response from FID/methanizer to CO at
483 high concentrations (> ~1.5%). In addition, it is essential to consider the decrease of
484 outlet gas flow rate caused by the neutralization of CO_2 with OH^- generated during the
485 cathodic reaction to eliminate the overestimation of gas fractions[54]. The reactions at the
486 cathode can be written as:

487 $$CO_2 + H_2O + 2\ e^- \rightarrow CO + 2\ OH^-$$

488 $$2\ CO_2 + 2\ OH^- \rightarrow 2\ HCO_3^-$$

489 A high-purity CO_2 (99.999%) gas flow at 20 sccm was delivered into the gas chamber
490 and went through the backside of cathode during reaction before entering the sample loop
491 of GC. The electrodes were electrolyzed at -10 mA cm^{-2} for 40 min to activate catalysts.
492 The electrodes were operated in constant-current mode (40 min for each current) to
493 obtain the potentials and Faradaic efficiencies at different current densities. For
494 electrodes exhibit unstable activities, the potentials were recorded at 20 min and
495 injections to GC were made at the same time to analyze product distributions.
496 Experiments using a three-compartment GDE cell with a 0.95 cm^2 active area and

497 flowing electrolytes (100 ml 1.0 M $KHCO_3$ pre-saturated with argon recycling through
498 the cathodic compartment by a peristaltic pump) gave similar results with the 0.5 cm^2
499 active area cell.

500 ***In-situ/Operando* XAS measurement**

501 *In-situ/Operando* XAS was performed at beamlines 5BM-D and 9-BM-B&C at the
502 Advanced Photon Source (APS) of Argonne National Laboratory (ANL). The working
503 electrodes were prepared by depositing 1.0 mg catalyst on a 2.5 × 1.5 cm^2 CFP (Toray,
504 TGP-H-060) to form a 0.5 × 1.0 cm^2 active area. The working electrode, counter
505 electrode (Pt) and reference electrode (Ag/AgCl) were mounted onto a custom-designed
506 XAS fluorescence cell[45,55]. All the electrochemical measurement was done by a CHI
507 760E potentiostat. A Vortex ME4 detector was used to collect fluorescence signals at Ni
508 K-edges. All XAS data analysis were performed with Athena and Artemis[56] to extract X-
509 ray absorption near edge structure (XANES) and extended X-ray absorption fine
510 structure (EXAFS) information.

511 **Computational details**

512 All DFT calculations on metal phthalocyanine molecules in this study were performed
513 using the Gaussian 09 program[57]. PBE0 functional[58] with D3 correction (Becke-Johnson
514 damping)[59] was adopted for its robustness and dispersion corrections, which make it
515 widely accepted as proper functional to study reaction of transition metal complexes[60].
516 The Stuttgart-Dresden (SDD) pseudopotential and double-ξ valence basis set were used
517 for transition metal atoms (Ni)[61]. For all other main group elements (H, C, N, O), the all-
518 electron 6-31G* basis set[62-64] was used. The geometric structures of all species were fully

519 optimized. Harmonic vibrational frequencies were also computed, whose result showed
520 that all reaction intermediates have no imaginary frequency. The gas-phase Gibbs free
521 energies (G) of high-spin and low-spin forms of all intermediates, *G*, were calculated
522 with the harmonic potential approximation at optimized structures at 298.15 K and under
523 1 atm to determine the ground states in realistic conditions. These ground state structures
524 were then used in the mechanism study.

525 Kohn-Sham molecular orbital analysis, Mayer bond order analysis, and atomic charge
526 analysis by modified Mulliken atom population defined by Bickelhaupt were performed
527 using Multiwfn software[65-68]. The 3D models of all reaction intermediates were
528 visualized using POV-Ray program[69].

529 The electrocatalytic mechanisms were studied based on Nørskov's computational
530 hydrogen electrode (CHE) model. This model provides an efficient approach to study
531 proton-electron transfer in electrocatalysis without treating solvated protons explicitly
532 and is widely used in theoretical study of electrocatalysis[70,71]. In this technique, zero
533 voltage was defined based on the reversible hydrogen electrode at all pH, *T*, and *p*.
534 Therefore, $\mu(H^+) + \mu(e^-) = \frac{1}{2}\mu(H_2)$ at a potential of 0 V. The effect of applied bias on
535 a proton-electron transfer step is represented by adding a $-eU$ term to the standard ΔG.
536 The pathways adopted for CO_2 reduction to CO in this work are listed below (* stands for
537 the active site):

538 $$* + CO_2 + H^+ + e^- \rightarrow *COOH$$

539 $$*COOH + H^+ + e^- \rightarrow *CO + H_2O$$

540 $$*CO \rightarrow * + CO$$

Data availability

The authors declare that the main data supporting the findings of this study are available within the article, its Supplementary Information, and Source Data.

Corresponding authors

Correspondence to Yongye Liang, Zhenxing Feng, or Yang-Gang Wang.

Acknowledgements

Y.L. acknowledges financial supports from Shenzhen fundamental research funding (JCYJ20160608140827794) and Guangdong-Hong Kong-Macao Joint Laboratory for Photonic-Thermal-Electrical Energy Materials and Devices (2019B121205001). H.W. acknowledges funding support from the US National Science Foundation (Grant CHE-1651717). Z.F. thanks the startup support from Oregon State University, USA. Y.G.W. acknowledges financial supports from Guangdong Provincial Key Laboratory of Catalysis (2020B121201002). J.L. is supported by National Natural Science Foundation of China (Grant No. 21590792, 91426302, and 21433005). The computational resource is supported from the Center for Computational Science and Engineering (SUSTech) and Tsinghua National Laboratory for Information Science and Technology. TEM, MS, and ICP data were obtained using equipment maintained by SUSTech Core Research Facilities. We acknowledge the technical support from Dr.

Richard Rosenberg at 4-ID, Advanced Photon Source (APS) of Argonne National Laboratory (ANL). XAS measurements were performed at 9-BM and DND-CAT 5-BM. The use of APS of ANL is supported by Department of Energy under Contract No. DE-AC02-06CH11357. DND-CAT is supported through E. I. duPont de Nemours & Co., Northwestern University, and The Dow Chemical Company.

Author Contributions

X.Z., Y.W., M.G., and M.W. contributed equally to this work. Y.L. and X.Z. conceived the project and designed the experiments. X.Z., Y.W., W.P., and Z.J. carried out the synthesis, material characterizations and electrochemical measurements. M.G. carried out the scanning transmission electron microscopy characterization. M.W., G.E.S., H.Z., M.L., Q.M., and Z.F. carried out the XAS characterizations. Z.Z., Y-G.W., and J.L. performed the DFT calculations. Y.L., X.Z., H.W., and H.D. analyzed the data. Y.L., X.Z. and H.D. prepared the manuscript with input from all the authors. All authors discussed the results and commented on the manuscript.

Competing Interests

The authors declare no competing interests.

Supporting information

Supplementary Figs. 1-31, Supplementary Tables 1-4, and Supplementary References 1-15.

References

1 Lewis, N. S. & Nocera, D. G. Powering the planet: Chemical challenges in solar energy utilization. *Proc. Natl. Acad. Sci. U.S.A.* **103**, 15729-15735, (2006).

2 Davis, S. J., Caldeira, K. & Matthews, H. D. Future CO_2 Emissions and Climate Change from Existing Energy Infrastructure. *Science* **329**, 1330-1333, (2010).

3 Artero, V. & Fontecave, M. Solar fuels generation and molecular systems: is it homogeneous or heterogeneous catalysis? *Chem. Soc. Rev.* **42**, 2338-2356, (2013).

4 Seh, Z. W., Kibsgaard, J., Dickens, C. F., Chorkendorff, I., Nørskov, J. K. & Jaramillo, T. F. Combining theory and experiment in electrocatalysis: Insights into materials design. *Science* **355**, eaad4998, (2017).

5 Gao, S., Lin, Y., Jiao, X., Sun, Y., Luo, Q., Zhang, W., Li, D., Yang, J. & Xie, Y. Partially oxidized atomic cobalt layers for carbon dioxide electroreduction to liquid fuel. *Nature* **529**, 68, (2016).

6 Dinh, C.-T., Burdyny, T., Kibria, M. G., Seifitokaldani, A., Gabardo, C. M., García de Arquer, F. P., Kiani, A., Edwards, J. P., De Luna, P., Bushuyev, O. S., Zou, C., Quintero-Bermudez, R., Pang, Y., Sinton, D. & Sargent, E. H. CO_2 electroreduction to ethylene via hydroxide-mediated copper catalysis at an abrupt interface. *Science* **360**, 783-787, (2018).

7 Fei, H., Dong, J., Feng, Y., Allen, C. S., Wan, C., Volosskiy, B., Li, M., Zhao, Z., Wang, Y., Sun, H., An, P., Chen, W., Guo, Z., Lee, C., Chen, D., Shakir, I., Liu, M., Hu, T., Li, Y., Kirkland, A. I., Duan, X. & Huang, Y. General synthesis and definitive structural identification of MN_4C_4 single-atom catalysts with tunable electrocatalytic activities. *Nat. Catal.* **1**, 63-72, (2018).

8 Kortlever, R., Shen, J., Schouten, K. J. P., Calle-Vallejo, F. & Koper, M. T. M. Catalysts and Reaction Pathways for the Electrochemical Reduction of Carbon Dioxide. *J. Phys. Chem. Lett.* **6**, 4073-4082, (2015).

9 Zheng, T., Jiang, K. & Wang, H. Recent Advances in Electrochemical CO_2-to-CO Conversion on Heterogeneous Catalysts. *Adv. Mater.* **30**, 1802066, (2018).

10 De Luna, P., Hahn, C., Higgins, D., Jaffer, S. A., Jaramillo, T. F. & Sargent, E. H. What would it take for renewably powered electrosynthesis to displace petrochemical processes? *Science* **364**, eaav3506, (2019).

11 Jiao, F., Li, J., Pan, X., Xiao, J., Li, H., Ma, H., Wei, M., Pan, Y., Zhou, Z., Li, M., Miao, S., Li, J., Zhu, Y., Xiao, D., He, T., Yang, J., Qi, F., Fu, Q. & Bao, X. Selective conversion of syngas to light olefins. *Science* **351**, 1065-1068, (2016).

12 Chen, Y., Li, C. W. & Kanan, M. W. Aqueous CO_2 Reduction at Very Low Overpotential on Oxide-Derived Au Nanoparticles. *J. Am. Chem. Soc.* **134**, 19969-19972, (2012).

13 Liu, M., Pang, Y., Zhang, B., De Luna, P., Voznyy, O., Xu, J., Zheng, X., Dinh, C. T., Fan, F., Cao, C., de Arquer, F. P. G., Safaei, T. S., Mepham, A., Klinkova, A., Kumacheva, E., Filleter, T., Sinton, D., Kelley, S. O. & Sargent, E. H. Enhanced electrocatalytic CO_2 reduction via field-induced reagent concentration. *Nature* **537**, 382-386, (2016).

14 Dinh, C.-T., García de Arquer, F. P., Sinton, D. & Sargent, E. H. High Rate, Selective, and Stable Electroreduction of CO_2 to CO in Basic and Neutral Media. *ACS Energy Lett.* **3**, 2835-2840, (2018).

15 Verma, S., Hamasaki, Y., Kim, C., Huang, W., Lu, S., Jhong, H.-R. M., Gewirth, A. A., Fujigaya, T., Nakashima, N. & Kenis, P. J. A. Insights into the Low Overpotential Electroreduction of CO_2 to CO on a Supported Gold Catalyst in an Alkaline Flow Electrolyzer. *ACS Energy Lett.* **3**, 193-198, (2018).

16 Jhong, H.-R. M., Ma, S. & Kenis, P. J. A. Electrochemical conversion of CO_2 to useful chemicals: current status, remaining challenges, and future opportunities. *Curr. Opin. Chem. Eng.* **2**, 191-199, (2013).

17 Zhao, C., Dai, X., Yao, T., Chen, W., Wang, X., Wang, J., Yang, J., Wei, S., Wu, Y. & Li, Y. Ionic Exchange of Metal–Organic Frameworks to Access Single Nickel Sites for Efficient Electroreduction of CO_2. *J. Am. Chem. Soc.* **139**, 8078-8081, (2017).

18 Ju, W., Bagger, A., Hao, G.-P., Varela, A. S., Sinev, I., Bon, V., Roldan Cuenya, B., Kaskel, S., Rossmeisl, J. & Strasser, P. Understanding activity and selectivity of metal-nitrogen-doped carbon catalysts for electrochemical reduction of CO_2. *Nat. Commun.* **8**, 944, (2017).

19 Lieber, C. M. & Lewis, N. S. Catalytic reduction of carbon dioxide at carbon electrodes modified with cobalt phthalocyanine. *J. Am. Chem. Soc.* **106**, 5033-5034, (1984).

20 Costentin, C., Drouet, S., Robert, M. & Savéant, J.-M. A Local Proton Source Enhances CO_2 Electroreduction to CO by a Molecular Fe Catalyst. *Science* **338**, 90-94, (2012).

21 Lin, S., Diercks, C. S., Zhang, Y.-B., Kornienko, N., Nichols, E. M., Zhao, Y., Paris, A. R., Kim, D., Yang, P., Yaghi, O. M. & Chang, C. J. Covalent organic frameworks comprising cobalt porphyrins for catalytic CO_2 reduction in water. *Science* **349**, 1208-1213, (2015).

22 Zhang, X., Wu, Z., Zhang, X., Li, L., Li, Y., Xu, H., Li, X., Yu, X., Zhang, Z., Liang, Y. & Wang, H. Highly selective and active CO_2 reduction electrocatalysts based on cobalt phthalocyanine/carbon nanotube hybrid structures. *Nat. Commun.* **8**, 14675, (2017).

23 Ren, S., Joulié, D., Salvatore, D., Torbensen, K., Wang, M., Robert, M. & Berlinguette, C. P. Molecular electrocatalysts can mediate fast, selective CO_2 reduction in a flow cell. *Science* **365**, 367-369, (2019).

24 Zhu, M., Ye, R., Jin, K., Lazouski, N. & Manthiram, K. Elucidating the Reactivity and Mechanism of CO_2 Electroreduction at Highly Dispersed Cobalt Phthalocyanine. *ACS Energy Lett.* **3**, 1381-1386, (2018).

25 Jiang, Z., Wang, Y., Zhang, X., Zheng, H., Wang, X. & Liang, Y. Revealing the hidden performance of metal phthalocyanines for CO_2 reduction electrocatalysis by hybridization with carbon nanotubes. *Nano Res.*, (2019).

26 Hu, X.-M., Rønne, M. H., Pedersen, S. U., Skrydstrup, T. & Daasbjerg, K. Enhanced Catalytic Activity of Cobalt Porphyrin in CO_2 Electroreduction upon Immobilization on Carbon Materials. *Angew. Chem. Int. Ed.* **56**, 6468-6472, (2017).
27 Zhu, M., Chen, J., Huang, L., Ye, R., Xu, J. & Han, Y.-F. Covalently Grafting Cobalt Porphyrin onto Carbon Nanotubes for Efficient CO_2 Electroreduction. *Angew. Chem. Int. Ed.* **58**, 6595-6599, (2019).
28 Choi, J., Wagner, P., Gambhir, S., Jalili, R., MacFarlane, D. R., Wallace, G. G. & Officer, D. L. Steric Modification of a Cobalt Phthalocyanine/Graphene Catalyst To Give Enhanced and Stable Electrochemical CO_2 Reduction to CO. *ACS Energy Lett.* **4**, 666-672, (2019).
29 Maurin, A. & Robert, M. Noncovalent Immobilization of a Molecular Iron-Based Electrocatalyst on Carbon Electrodes for Selective, Efficient CO_2-to-CO Conversion in Water. *J. Am. Chem. Soc.* **138**, 2492-2495, (2016).
30 Wu, Y., Jiang, Z., Lu, X., Liang, Y. & Wang, H. Domino electroreduction of CO_2 to methanol on a molecular catalyst. *Nature* **575**, 639-642, (2019).
31 Li, X., Bi, W., Chen, M., Sun, Y., Ju, H., Yan, W., Zhu, J., Wu, X., Chu, W., Wu, C. & Xie, Y. Exclusive Ni–N_4 Sites Realize Near-Unity CO Selectivity for Electrochemical CO_2 Reduction. *J. Am. Chem. Soc.* **139**, 14889-14892, (2017).
32 Yang, H. B., Hung, S.-F., Liu, S., Yuan, K., Miao, S., Zhang, L., Huang, X., Wang, H.-Y., Cai, W., Chen, R., Gao, J., Yang, X., Chen, W., Huang, Y., Chen, H. M., Li, C. M., Zhang, T. & Liu, B. Atomically dispersed Ni(I) as the active site for electrochemical CO_2 reduction. *Nat. Energy* **3**, 140-147, (2018).
33 Yan, C., Li, H., Ye, Y., Wu, H., Cai, F., Si, R., Xiao, J., Miao, S., Xie, S., Yang, F., Li, Y., Wang, G. & Bao, X. Coordinatively unsaturated nickel–nitrogen sites towards selective and high-rate CO_2 electroreduction. *Energy Environ. Sci.* **11**, 1204-1210, (2018).
34 Jiang, K., Siahrostami, S., Zheng, T., Hu, Y., Hwang, S., Stavitski, E., Peng, Y., Dynes, J., Gangisetty, M., Su, D., Attenkofer, K. & Wang, H. Isolated Ni single atoms in graphene nanosheets for high-performance CO_2 reduction. *Energy Environ. Sci.* **11**, 893-903, (2018).
35 Sorokin, A. B. Phthalocyanine Metal Complexes in Catalysis. *Chem. Rev.* **113**, 8152-8191, (2013).
36 Zhang, Z., Xiao, J., Chen, X.-J., Yu, S., Yu, L., Si, R., Wang, Y., Wang, S., Meng, X., Wang, Y., Tian, Z.-Q. & Deng, D. Reaction Mechanisms of Well-Defined Metal–N_4 Sites in Electrocatalytic CO_2 Reduction. *Angew. Chem. Int. Ed.* **57**, 16339-16342, (2018).
37 Clark, E. L., Resasco, J., Landers, A., Lin, J., Chung, L.-T., Walton, A., Hahn, C., Jaramillo, T. F. & Bell, A. T. Standards and Protocols for Data Acquisition and Reporting for Studies of the Electrochemical Reduction of Carbon Dioxide. *ACS Catal.* **8**, 6560-6570, (2018).
38 Weekes, D. M., Salvatore, D. A., Reyes, A., Huang, A. & Berlinguette, C. P. Electrolytic CO_2 Reduction in a Flow Cell. *Acc. Chem. Res.* **51**, 910-918, (2018).
39 Higgins, D., Hahn, C., Xiang, C., Jaramillo, T. F. & Weber, A. Z. Gas-Diffusion Electrodes for Carbon Dioxide Reduction: A New Paradigm. *ACS Energy Lett.* **4**, 317-324, (2019).

40 Yin, Z., Peng, H., Wei, X., Zhou, H., Gong, J., Huai, M., Xiao, L., Wang, G., Lu, J. & Zhuang, L. An alkaline polymer electrolyte CO_2 electrolyzer operated with pure water. *Energy Environ. Sci.* **12**, 2455-2462, (2019).
41 Möller, T., Ju, W., Bagger, A., Wang, X., Luo, F., Ngo Thanh, T., Varela, A. S., Rossmeisl, J. & Strasser, P. Efficient CO_2 to CO electrolysis on solid Ni–N–C catalysts at industrial current densities. *Energy Environ. Sci.* **12**, 640-647, (2019).
42 Kutz, R. B., Chen, Q., Yang, H., Sajjad, S. D., Liu, Z. & Masel, I. R. Sustainion Imidazolium-Functionalized Polymers for Carbon Dioxide Electrolysis. *Energy Technol.* **5**, 929-936, (2017).
43 Wang, M., Torbensen, K., Salvatore, D., Ren, S., Joulié, D., Dumoulin, F., Mendoza, D., Lassalle-Kaiser, B., Işci, U., Berlinguette, C. P. & Robert, M. CO_2 electrochemical catalytic reduction with a highly active cobalt phthalocyanine. *Nat. Commun.* **10**, 3602, (2019).
44 Wu, Y., Jiang, J., Weng, Z., Wang, M., Broere, D. L. J., Zhong, Y., Brudvig, G. W., Feng, Z. & Wang, H. Electroreduction of CO_2 Catalyzed by a Heterogenized Zn–Porphyrin Complex with a Redox-Innocent Metal Center. *ACS Cent. Sci.* **3**, 847-852, (2017).
45 Weng, Z., Wu, Y., Wang, M., Jiang, J., Yang, K., Huo, S., Wang, X.-F., Ma, Q., Brudvig, G. W., Batista, V. S., Liang, Y., Feng, Z. & Wang, H. Active sites of copper-complex catalytic materials for electrochemical carbon dioxide reduction. *Nat. Commun.* **9**, 415, (2018).
46 Rollmann, L. D. & Iwamoto, R. T. Electrochemistry, electron paramagnetic resonance, and visible spectra of cobalt, nickel, copper, and metal-free phthalocyanines in dimethyl sulfoxide. *J. Am. Chem. Soc.* **90**, 1455-1463, (1968).
47 Chen, L. X., Jäger, W. J. H., Jennings, G., Gosztola, D. J., Munkholm, A. & Hessler, J. P. Capturing a Photoexcited Molecular Structure Through Time-Domain X-ray Absorption Fine Structure. *Science* **292**, 262-264, (2001).
48 Yamamoto, T. Assignment of pre-edge peaks in K-edge x-ray absorption spectra of 3d transition metal compounds: electric dipole or quadrupole? *X-ray Spectrom.* **37**, 572-584, (2008).
49 Froehlich, J. D. & Kubiak, C. P. The Homogeneous Reduction of CO_2 by $[Ni(cyclam)]^+$: Increased Catalytic Rates with the Addition of a CO Scavenger. *J. Am. Chem. Soc.* **137**, 3565-3573, (2015).
50 Costentin, C. & Savéant, J.-M. Towards an intelligent design of molecular electrocatalysts. *Nat. Rev. Chem.* **1**, 0087, (2017).
51 Kim, S.-J., Matsumoto, M. & Shigehara, K. Synthesis and electrical properties of poly(μ-1,4-diisocyanobenzene) octacyanophthalocyaninatoiron(II). *Synth. Met.* **107**, 27-33, (1999).
52 Yslas, E. I., Rivarola, V. & Durantini, E. N. Synthesis and photodynamic activity of zinc(II) phthalocyanine derivatives bearing methoxy and trifluoromethylbenzyloxy substituents in homogeneous and biological media. *Bioorg. Med. Chem.* **13**, 39-46, (2005).
53 Kim, S.-J., Matsumoto, M. & Shigehara, K. Synthesis and electrical properties of one-dimensional octacyanometallophthalocyanine (M≡Fe, Co) polymers. *J Porphyr. Phthalocyanines* **04**, 136-144, (2000).

54 Ma, M., Clark, E. L., Therkildsen, K. T., Dalsgaard, S., Chorkendorff, I. & Seger, B. Insights into the carbon balance for CO_2 electroreduction on Cu using gas diffusion electrode reactor designs. *Energy Environ. Sci.* **13**, 977-985, (2020).
55 Wang, M., Árnadóttir, L., Xu, Z. J. & Feng, Z. In Situ X-ray Absorption Spectroscopy Studies of Nanoscale Electrocatalysts. *Nano-Micro Lett.* **11**, 47, (2019).
56 Ravel, B. & Newville, M. ATHENA, ARTEMIS, HEPHAESTUS: data analysis for X-ray absorption spectroscopy using IFEFFIT. *J. Synchrotron Radiat.* **12**, 537-541, (2005).
57 Frisch, M. J., et al. Gaussian 09, Gaussian, Inc., Wallingford CT, 2009.
58 Adamo, C. & Barone, V. Toward reliable density functional methods without adjustable parameters: The PBE0 model. *J. Chem. Phys.* **110**, 6158-6170, (1999).
59 Grimme, S., Ehrlich, S. & Goerigk, L. Effect of the damping function in dispersion corrected density functional theory. *J. Comput. Chem.* **32**, 1456-1465, (2011).
60 Steinmetz, M. & Grimme, S. Benchmark Study of the Performance of Density Functional Theory for Bond Activations with (Ni,Pd)-Based Transition-Metal Catalysts. *ChemistryOpen* **2**, 115-124, (2013).
61 Andrae, D., Häußermann, U., Dolg, M., Stoll, H. & Preuß, H. Energy-adjusted ab initio pseudopotentials for the second and third row transition elements. *Theor. Chim. Acta* **77**, 123-141, (1990).
62 Hariharan, P. C. & Pople, J. A. The influence of polarization functions on molecular orbital hydrogenation energies. *Theor. Chim. Acta* **28**, 213-222, (1973).
63 Gordon, M. S. The isomers of silacyclopropane. *Chem. Phys. Lett.* **76**, 163-168, (1980).
64 Binning, R. & Curtiss, L. Compact contracted basis sets for third-row atoms: Ga-Kr. *J. Comput. Chem.* **11**, 1206-1216, (1990).
65 Hirshfeld, F. L. Bonded-atom fragments for describing molecular charge densities. *Theor. Chim. Acta* **44**, 129-138, (1977).
66 Lu, T. & Chen, F. Calculation of molecular orbital composition. *Acta Chim. Sinica* **69**, 2393-2406, (2011).
67 Mayer, I. Charge, bond order and valence in the AB initio SCF theory. *Chem. Phys. Lett.* **97**, 270-274, (1983).
68 Lu, T. & Chen, F. Multiwfn: A multifunctional wavefunction analyzer. *J. Comput. Chem.* **33**, 580-592, (2012).
69 Buck, D. & Collins, A. *POV-Ray - The Persistence of Vision Raytracer*.
70 Chan, K. & Nørskov, J. K. Electrochemical Barriers Made Simple. *J. Phys. Chem. Lett.* **6**, 2663-2668, (2015).
71 Peterson, A. A., Abild-Pedersen, F., Studt, F., Rossmeisl, J. & Nørskov, J. K. How copper catalyzes the electroreduction of carbon dioxide into hydrocarbon fuels. *Energy Environ. Sci.* **3**, 1311-1315, (2010).

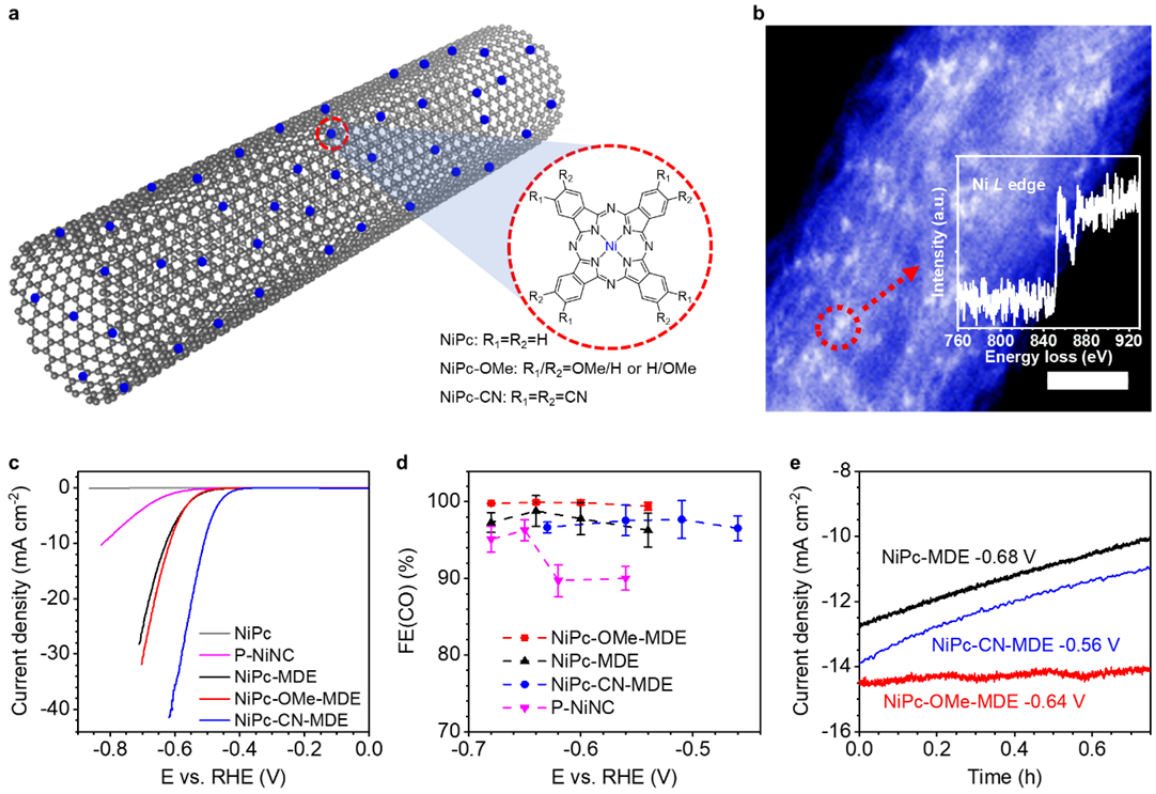

Fig. 1: Structure and CO_2RR performance of NiPc-MDEs. **a**, Schematic presentation of the NiPc-MDEs with NiPc molecules anchored on the side wall of MWCNTs. Inset shows the molecular structures of NiPc, NiPc-OMe, and NiPc-CN. **b**, Z-contrast HADDF-STEM image of NiPc-OMe-MDE and the EELS spectrum at the Ni *L* edge of the circled bright spots (inset). Scale bar: 2 nm. **c**, LSV of neat NiPc, P-NiNC, NiPc-MDE, NiPc-OMe-MDE, and NiPc-CN-MDE in CO_2-saturated 0.5 M $KHCO_3$ electrolyte after activation. Scan rate: 5 mV/s. **d**, FE(CO) of NiPc-OMe-MDE, NiPc-MDE, NiPc-CN-MDE, and P-NiNC at different applied potentials. The error bars represent standard deviations of three measurements and the dashed lines are guides to the eye. **e**, Chronoamperometry of the NiPc-MDE at -0.68 V, NiPc-CN-MDE at -0.56 V, and NiPc-OMe-MDE at -0.64 V. The stability of NiPc-MDE and NiPc-CN-MDE at high reduction currents is not ideal.

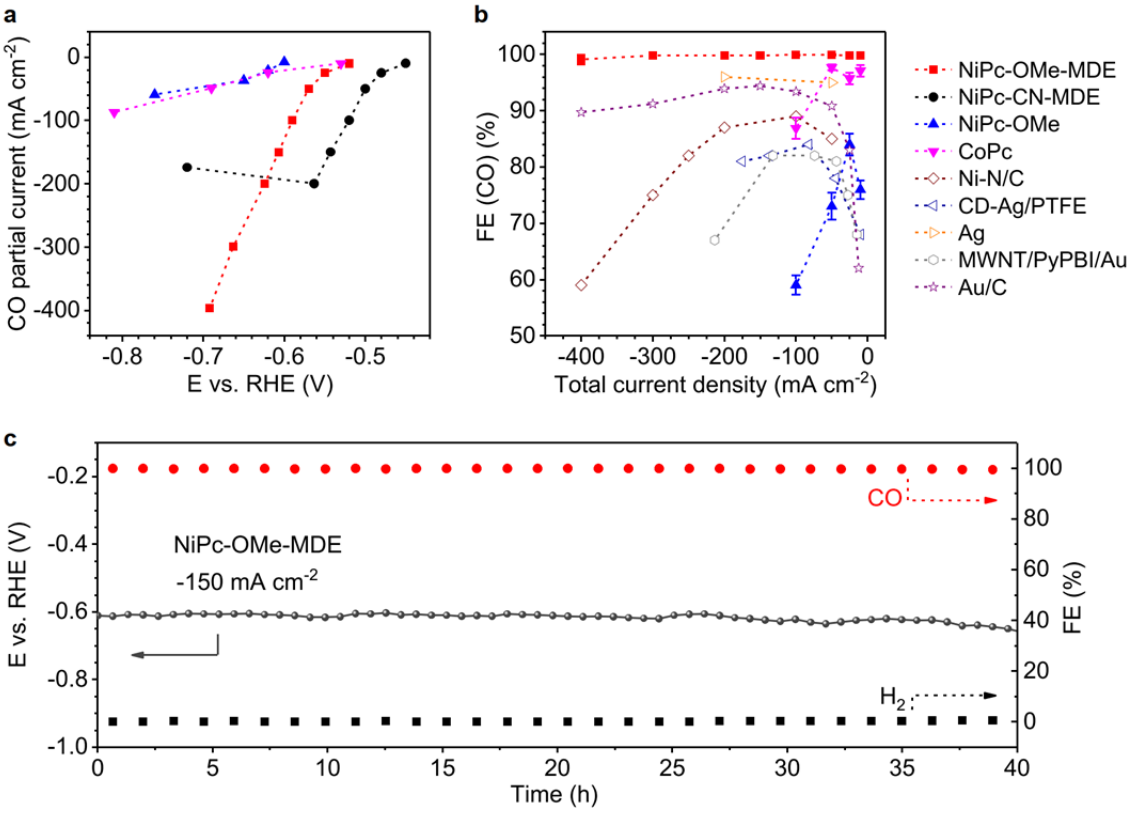

Fig. 2: GDEs with NiPc-MDEs. **a**, CO partial current of NiPc-OMe-MDE, NiPc-CN-MDE, NiPc-OMe, and CoPc at different potentials in 1 M $KHCO_3$ electrolyte. The dashed lines are guides to the eye. **b**, FE(CO) of NiPc-OMe-MDE, NiPc-OMe, CoPc and reported Ni-N/C[41], CD-Ag/PTFE[14], Ag[42], MWNT/PyPBI/Au[15], and Au/C[40] catalysts at different total current densities. The error bars represent standard deviations of three measurements and the dashed lines are guides to the eye. **c**, Long-term operation of NiPc-OMe-MDE at -150 mA cm^{-2}.

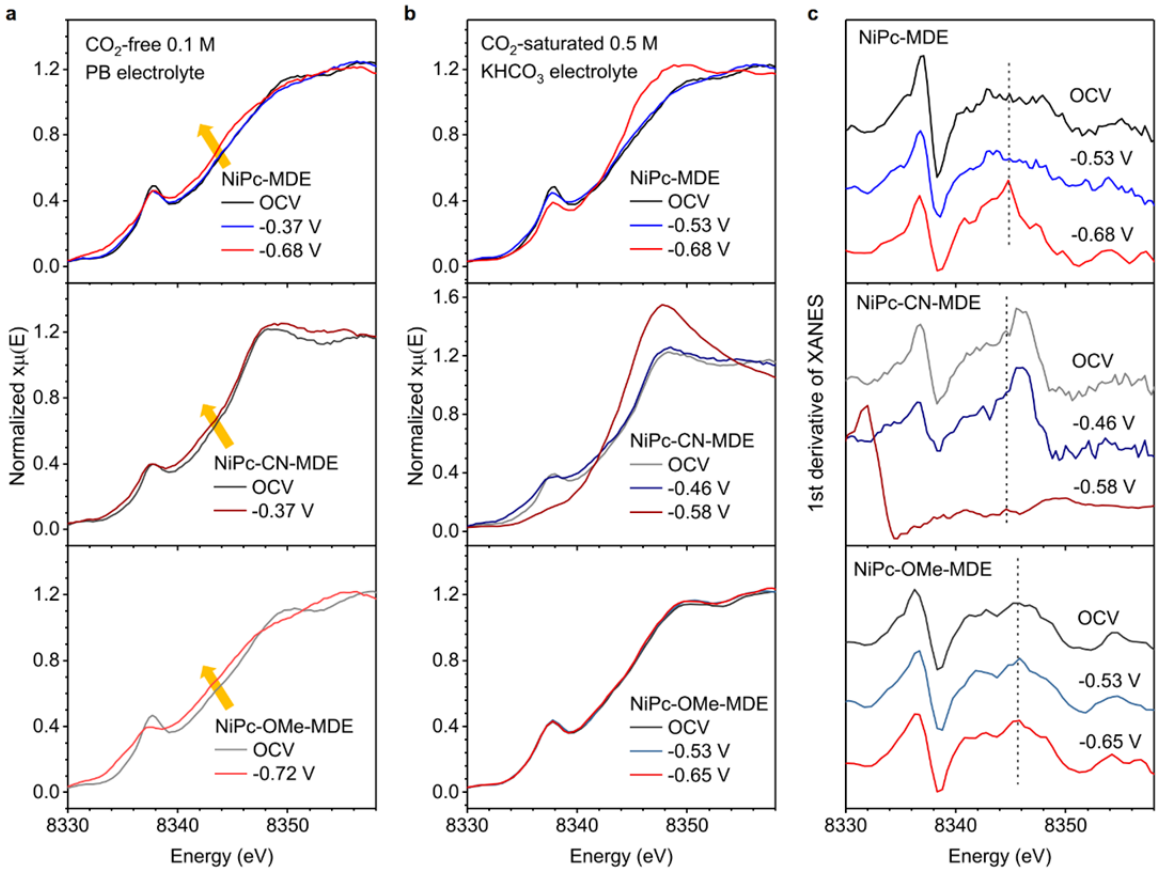

Fig. 3: *In-situ/operando* XAS of NiPc-MDEs. **a**, Normalized *in-situ* Ni K-edge XANES spectra of NiPc-MDE, NiPc-CN-MDE, and NiPc-OMe-MDE in CO_2-free (Ar-saturated) 0.1 M phosphate buffer. The yellow arrows show the red-shift of edges, indicating reduction of the Ni centers upon applying cathodic bias. **b**, Normalized *operando* Ni K-edge XANES spectra of NiPc-MDE, NiPc-CN-MDE, and NiPc-OMe-MDE at OCV and potentials with initial current densities of ~ -1 (less negative potentials) and ~ -5 mA cm^{-2} (more negative potentials) in CO_2-saturated 0.5 M $KHCO_3$. **c**, First derivatives of the spectra in **b**. The dashed lines show the peak positions of NiPc-MDEs at the most negative measured potentials.

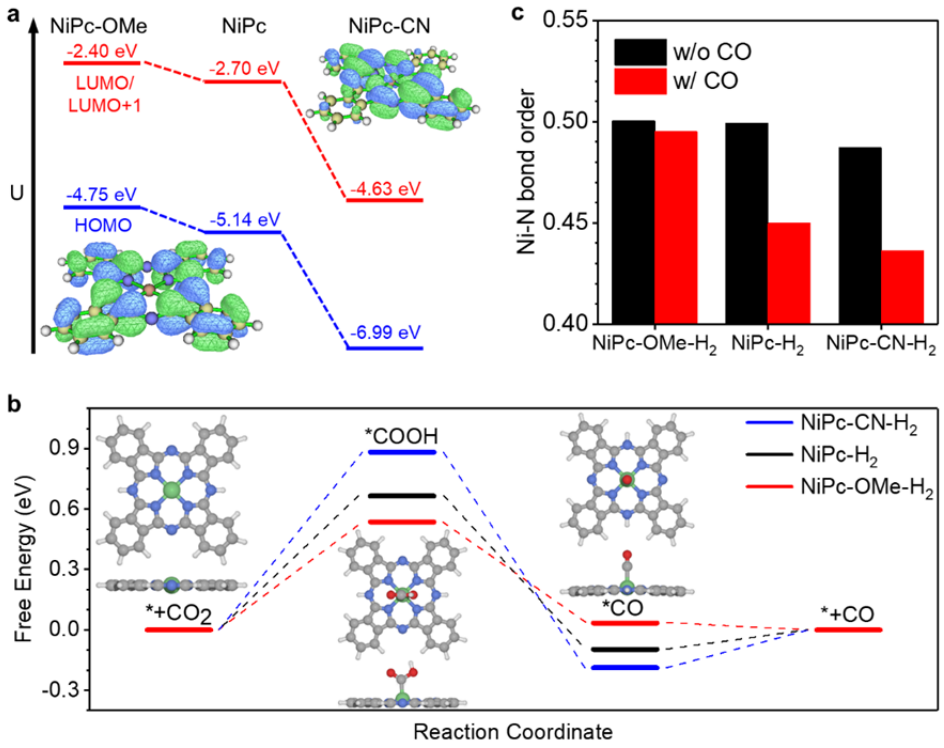

Fig. 4: DFT calculations of original and substituted NiPcs catalyzing CO_2RR. **a**, Calculated electron density distribution of HOMO and doubly degenerated LUMO/LUMO+1 of NiPc and the energy levels of HOMO and LUMO/LUMO+1 of NiPc-OMe, NiPc, and NiPc-CN. **b**, Calculated free energy diagram of NiPc-CN-H_2, NiPc-H_2, and NiPc-OMe-H_2 catalyzing CO_2RR at -0.11 V vs. RHE. Insets show the optimized configurations of intermediates with the NiPc-H_2 catalyst. The white, gray, blue, red, and green spheres in inset pictures represent H, C, N, O, and Ni, respectively. **c**, Ni-N bond orders of NiPc-OMe-H_2, NiPc-H_2, and NiPc-CN-H_2 without and with adsorbed CO. NiPc-OMe shows the strongest Ni-N bond, which could enhance its stability in CO_2RR.

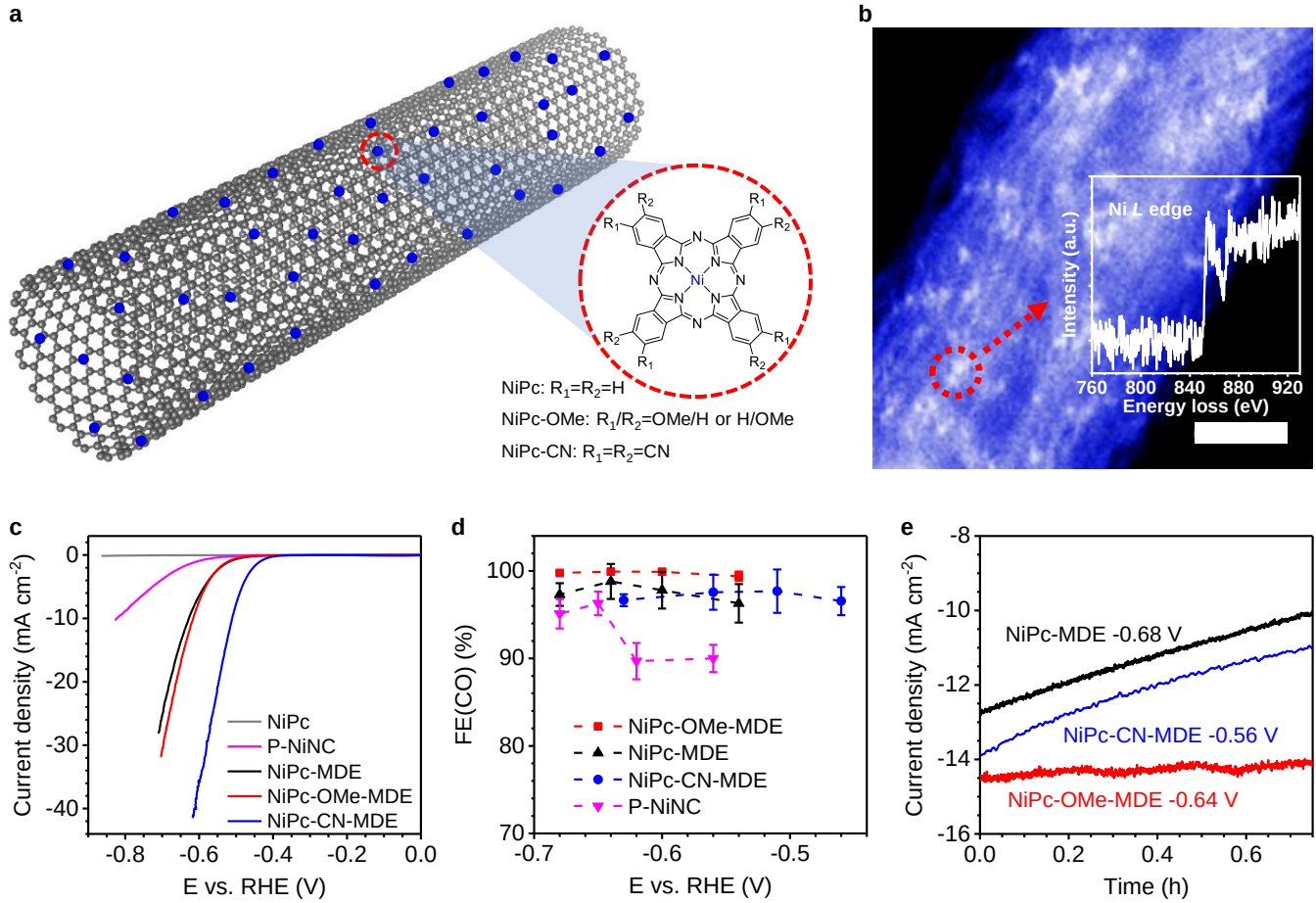
a
b
Ni L edge
Intensity (a.u.)
760 800 840 880 920
Energy loss (eV)
NiPc: R1=R2=H
NiPc-OMe: R1/R2=OMe/H or H/OMe
NiPc-CN: R1=R2=CN
c
Current density (mA cm-2)
E vs. RHE (V)
NiPc
P-NiNC
NiPc-MDE
NiPc-OMe-MDE
NiPc-CN-MDE
d
FE(CO) (%)
E vs. RHE (V)
NiPc-OMe-MDE
NiPc-MDE
NiPc-CN-MDE
P-NiNC
e
Current density (mA cm-2)
Time (h)
NiPc-MDE -0.68 V
NiPc-CN-MDE -0.56 V
NiPc-OMe-MDE -0.64 V

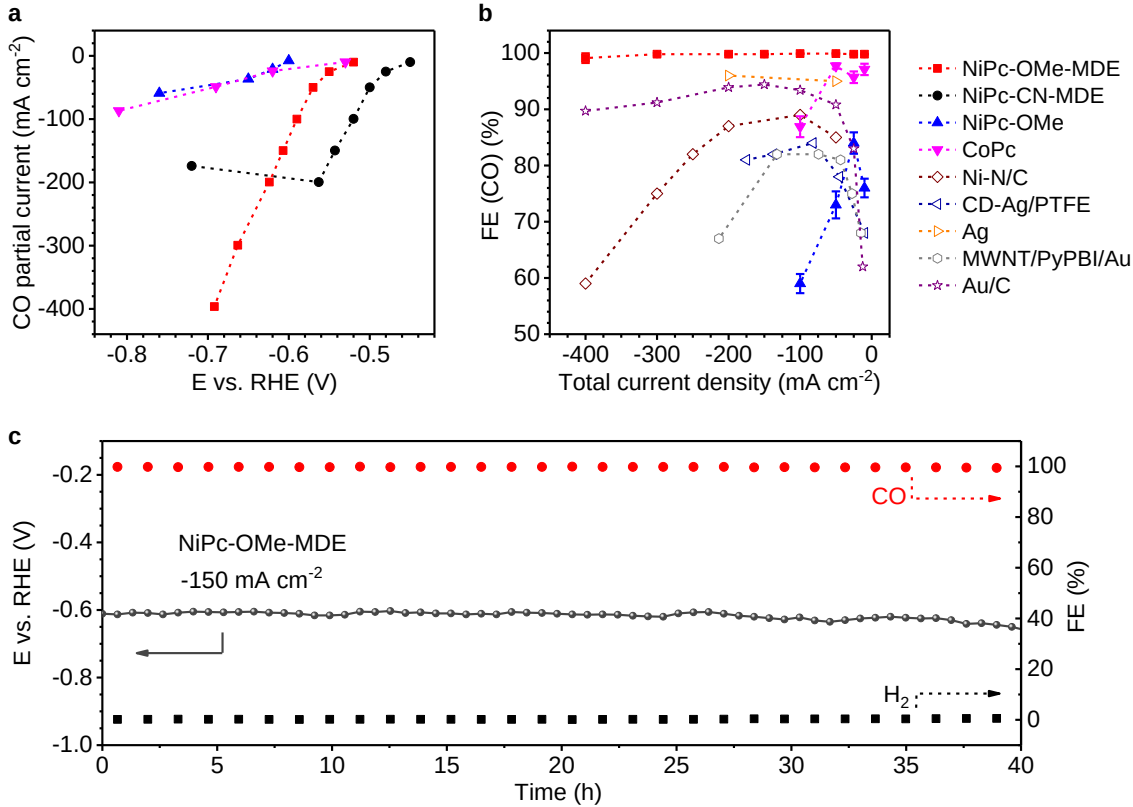
a
CO partial current (mA cm-2)
0
-100
-200
-300
-400
-0.8
-0.7
-0.6
-0.5
E vs. RHE (V)
b
FE (CO) (%)
100
90
80
70
60
50
-400
-300
-200
-100
0
Total current density (mA cm-2)
NiPc-OMe-MDE
NiPc-CN-MDE
NiPc-OMe
CoPc
Ni-N/C
CD-Ag/PTFE
Ag
MWNT/PyPBI/Au
Au/C
c
E vs. RHE (V)
-0.2
-0.4
-0.6
-0.8
-1.0
NiPc-OMe-MDE
-150 mA cm-2
CO
H2
100
80
60
40
20
0
FE (%)
0
5
10
15
20
25
30
35
40
Time (h)

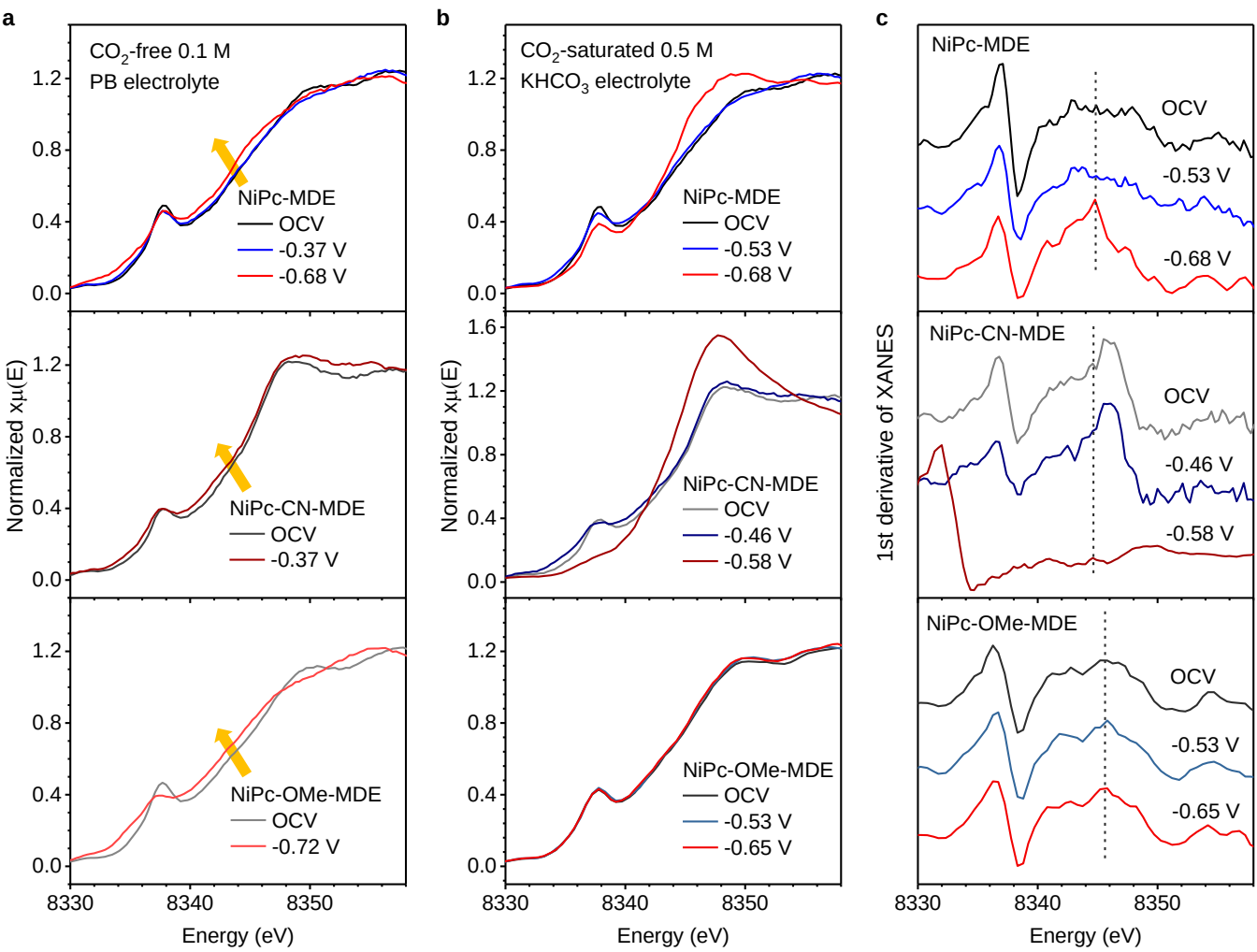
a
CO2-free 0.1 M
PB electrolyte
NiPc-MDE
OCV
-0.37 V
-0.68 V
NiPc-CN-MDE
OCV
-0.37 V
NiPc-OMe-MDE
OCV
-0.72 V
Normalized xμ(E)
Energy (eV)
b
CO2-saturated 0.5 M
KHCO3 electrolyte
NiPc-MDE
OCV
-0.53 V
-0.68 V
NiPc-CN-MDE
OCV
-0.46 V
-0.58 V
NiPc-OMe-MDE
OCV
-0.53 V
-0.65 V
Normalized xμ(E)
Energy (eV)
c
NiPc-MDE
OCV
-0.53 V
-0.68 V
NiPc-CN-MDE
OCV
-0.46 V
-0.58 V
NiPc-OMe-MDE
OCV
-0.53 V
-0.65 V
1st derivative of XANES
Energy (eV)

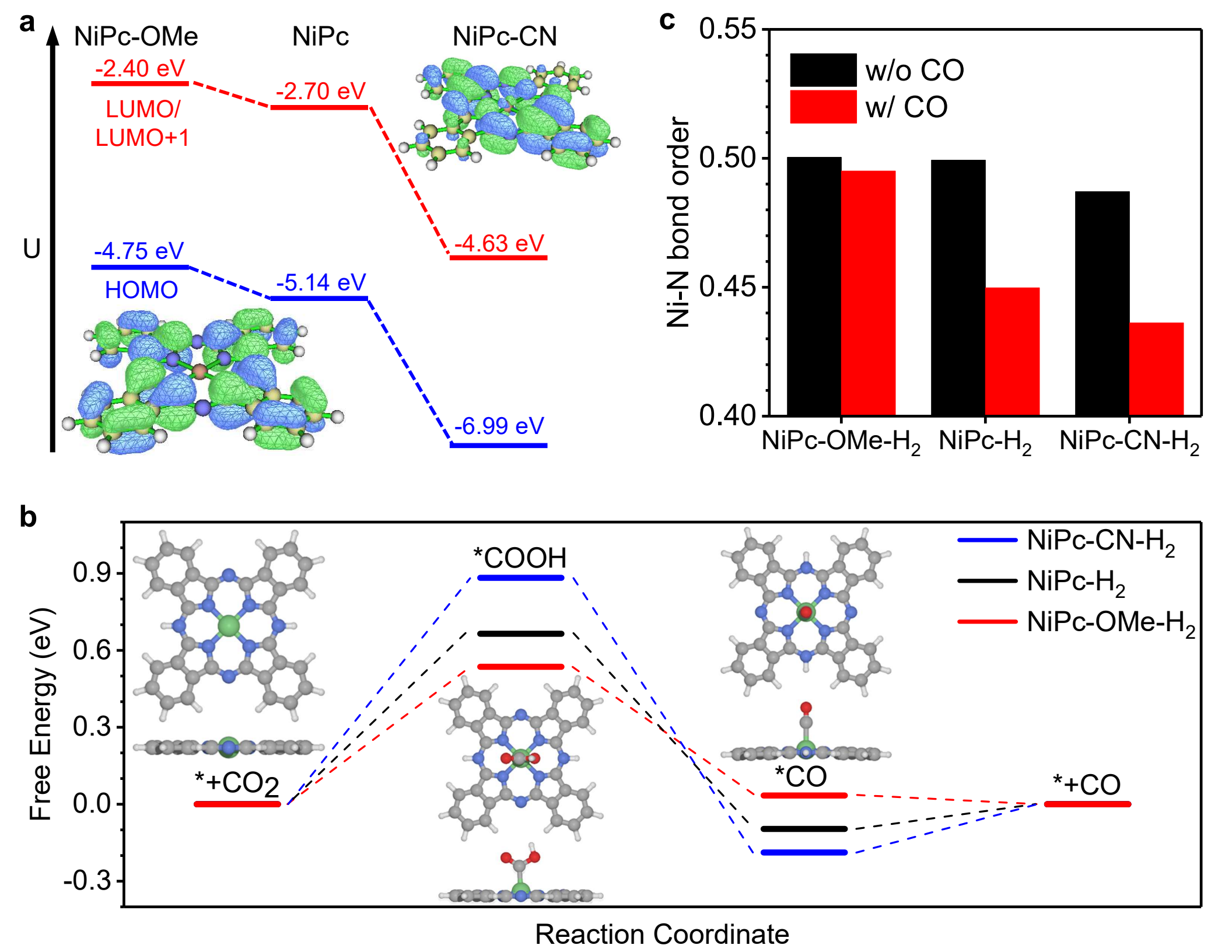
a
NiPc-OMe
NiPc
NiPc-CN
-2.40 eV
-2.70 eV
LUMO/
LUMO+1
-4.63 eV
U
-4.75 eV
-5.14 eV
HOMO
-6.99 eV
c
0.55
0.50
0.45
0.40
Ni-N bond order
w/o CO
w/ CO
NiPc-OMe-H2
NiPc-H2
NiPc-CN-H2
b
0.9
0.6
0.3
0.0
-0.3
Free Energy (eV)
*COOH
*+CO2
*CO
*+CO
NiPc-CN-H2
NiPc-H2
NiPc-OMe-H2
Reaction Coordinate